Open Archive TOULOUSE Archive Ouverte (OATAO)

OATAO is an open access repository that collects the work of Toulouse researchers and makes it freely available over the web where possible.

Any correspondance concerning this service should be sent to the repository administrator: staff-oatao@listes-diff.inp-toulouse.fr

Chemical Vapor Deposition of Al$_{13}$Fe$_4$ Highly Selective Catalytic Films for the Semi-Hydrogenation of Acetylene

Ioannis G. Aviziotis, Thomas Duguet, Khaled Soussi, Marc Heggen, Marie-Christine Lafont, Franck Morfin, Shashank Mishra, Stephane Daniele, Andreas G. Boudouvis, and Constantin Vahlas*

Catalytic properties of coatings containing the Al$_{13}$Fe$_4$ intermetallic phase are tested in the reaction of semi-hydrogenation of acetylene. The selectivity to ethylene is found as high as 74% close to the reported values for pure, unsupported Al$_{13}$Fe$_4$. The initial conversion of acetylene to ethylene is 84% and rapidly drops due to the catalytic formation of carbon-based by-products on secondary Al-Fe phases. Coatings are processed through sequential chemical vapor deposition (CVD) of aluminum (5 Torr, 180 °C) and iron (40 Torr, 140 °C) layers, followed by in situ annealing for 60 min at 575 °C. Deposition proceeds at high growth rate, resulting in 15 μm thick films. After annealing, coatings are composed of the Al$_{13}$Fe$_4$ phase, co-existing with minor secondary Al-Fe intermetallic phases. Overall, it is shown that films containing complex Al-Fe intermetallic phases can be processed by CVD, opening new routes to the engineering of pure, supported Al$_{13}$Fe$_4$ catalysts on 3D or porous supports.

1. Introduction

When ethylene, a major building block in the polymers industry,[1] is produced by the steam cracking method, the process suffers from the pollution by acetylene which acts as a

Dr. I. G. Aviziotis, Prof. A. G. Boudouvis
School of Chemical Engineering
National Technical University of Athens
Heroon Polytechniou 9, 15780 Zografou, Greece

Dr. I. G. Aviziotis, Dr. T. Duguet, Dr. M.-C. Lafont Dr. C. Vahlas
CIRIMAT
Université de Toulouse − CNRS
4 alleé Emile Monso, BP44362, 31030 Toulouse cedex 4, France
E-mail: constantin.vahlas@ensiacet.fr

Dr. K. Soussi, Prof. S. Mishra, F. Morfin, Prof. S. Daniele
IRCELYON
Université Lyon 1−CNRS
2 Avenue Albert Einstein, 69626 Villeurbanne cedex, France

Dr. M. Heggen
Ernst Ruska-Centrum und Peter Grünberg Institut
Forschungszentrum Jülich
Wilhelm-Johnen-Straße, 52428 Jülich, Germany

poison for the downstream polymerization catalyst.[2] Therefore, the removal of acetylene from ethylene streams is of paramount importance. Its semi-hydrogenation is performed by noble metal catalysts which are active at mild conditions but not always selective toward the targeted product.[3] The intermetallic compound Al$_{13}$Fe$_4$ (usually called Al$_3$Fe[4,5]), is composed of common metals and shows excellent selectivity in semi-hydrogenation of alkynes.[6] The high potential of Al$_{13}$Fe$_4$ to replace Pt and Pd noble metals or their intermetallic phases[6,7] in this catalytic process is due to its crystal structure, where Fe atoms are coordinated by Al atoms, and the arrangement of Fe-Al-Fe groups in 3D Al cavities[8] results in potential Fe catalytic sites according to the site-isolation concept.[6] Therefore, the implementation of Al$_{13}$Fe$_4$ catalysts in industrial heterogeneous reactions is expected to meet two prerequisites: (a) the replacement of expensive and rare noble metals, (b) the improvement of catalytic processes through increased selectivity.[9]

Several studies have been reported on the formation of intermetallic phases in the Al–Fe system.[10,11] Various deposition techniques have been applied to obtain Al-Fe intermetallic coatings, including thermal spraying and magnetron sputtering[11,12] or mechanical alloying.[13] Despite the effective production of Al-Fe intermetallics, these methods suffer a number of drawbacks, such as the swelling phenomenon because of rapid and violent phase transformations during sintering, or technical difficulties related to considerable differences of properties of the substrate and the coating materials (e.g., their coefficient of thermal expansion and reactivity resulting in a poor interfacial adherence). Furthermore, catalytic processes require high catalyst surface to volume ratio and for this reason, processing of Al-Fe films on supports (such as powders or preforms) is foreseen and may strengthen the catalytic performance of the intermetallic compound.[6]

Unfortunately, there is no established scalable and economic process for the production of Al$_{13}$Fe$_4$ catalysts with high specific surface area. The present work is a first step in this direction. By operating at relatively low to moderate temperatures; that is, in the limits of the reaction-limited regime, chemical vapor

deposition (CVD) can meet the requirements for the processing of Al-Fe coatings on complex, non-line-of-sight surfaces and powders such as honeycomb structures and gamma alumina catalytic supports, due to the predominance of the reaction kinetics over the transport phenomena.[14] Despite these advantages, there are but few reports on the processing of intermetallic phases by CVD,[15] mainly due to the complicated coupling of the chemistry of the different organometallic precursors involved in the process.

The attempts of formation of iron aluminides by CVD mostly involve high temperature diffusion processes on iron and steels substrates.[16] Targeted applications are then oxidation and/or corrosion resistance, calling for compact microstructures of the aluminide film. This contrasts with the specifications of films used in catalytic applications, where high specific surface area is desired.

In this paper, we describe an innovative route for the processing of $Al_{13}Fe_4$ films by sequential CVD of the two metals followed by in situ thermal annealing to stimulate reactive diffusion. This work is based on our recent investigations of the kinetics and the transport phenomena of the CVD of unary Al[17,18] and Fe.[19] We characterize the structure and composition of the films, we report preliminary results on the semi-hydrogenation of acetylene with the obtained Al-Fe films as catalysts and we propose correlations between the catalytic behavior and the characteristics of the films.

2. Results and Discussion

2.1. Films Structure and Composition

The as-processed coatings present a uniform mat gray color all over the surface of the substrates. **Figure 1** presents the XRD pattern of the annealed bilayer stack at 575 °C. It is compared with the $Al_{13}Fe_4$ XRD pattern adapted from a previous reference.[5] Reflections at low 2θ angles, between 20° and 30° as well as the large peaks between 40° and 50° and some smaller ones at higher 2θ angles (see full arrows in Figure 1) are characteristic of the monoclinic $Al_{13}Fe_4$ phase.

Other peaks, indicated by dashed and dotted arrows in Figure 1 do not match the $Al_{13}Fe_4$ pattern, revealing that other phases co-exist with $Al_{13}Fe_4$. Specifically, the peak at 39° − 40 ° can be attributed to the Al_5Fe_2 phase and to elemental Al (JCPDS cards no. 29–0043 and 04–0787, respectively). The peak at 50° is indexed to the Al_5Fe_2 phase. The intensity of the peak at approx. 45° implies that there still exists unreacted Fe within the film (JCPDS card no. 87–0722). The peak at 82° matches well both the *fcc* Al and the *bcc* Fe crystalline structures whereas the two last peaks at approx. 112° and 117° correspond to *fcc* Al alone.

Radio frequency glow discharge optical emission spectroscopy (GD-OES), X-ray photoelectron spectrometry (XPS) and transmission electron microscopy (TEM) are used to monitor composition uniformity, to confirm the formation of $Al_{13}Fe_4$ and to identify secondary phases, and finally to get a better insight into the film microstructure.

Figure 2 presents GD-OES qualitative Al, C, Fe, O composition profiles through the film thickness. The Al and Fe profiles are spread through the entire thickness revealing that intermixing
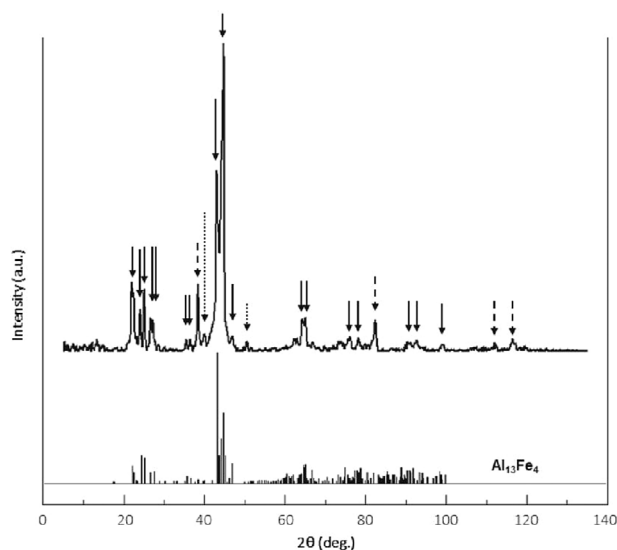

Figure 1. XRD pattern of the annealed coating (top) and diffraction pattern of the $Al_{13}Fe_4$ phase (bottom) adapted from previous works.[5] Full arrows point on $Al_{13}Fe_4$ peaks, whereas dashed and dotted arrows point on Al and Al_5Fe_2 peaks, respectively. The most intense peak at ca. 45° also corresponds to *fcc* Fe.

between Al and Fe occurs during the in situ annealing without achieving homogeneous composition along the thickness of the stack in the annealing conditions applied. The Fe concentration increases from the surface of the film to the interface with the substrate, despite the fact that it is deposited on the outer part of the bilayer, on the surface of the Al film. Inversely, the Al:Fe ratio decreases from the area close to the surface toward the substrate (Figure 2a). This observation is in agreement with results reported by Naoi et al.,[20] following which, the formation of stable intermetallic phases in the binary Al-Fe system occurs at the interface with the substrate in the temperature range 550–640 °C. The decrease of the Al:Fe ratio through the film toward the substrate is further confirmed by TEM and STEM/EDX discussed hereafter. O and C contamination remains low within the film. Indeed, by zooming in at the surface level (Figure 2b, sputtering time lower than 40 s), it can be observed that O and C heteroatoms are located at the surface and can be considered as superficial contaminants.

XPS is now used for the characterization of the surface composition. The initial surface composition of the as-processed film exposed to ambient air is Al(12.7)Fe(2.3)O(66.0)C(19) in at.%. This surface composition is the one relevant to the initial condition of the catalysis test. Nevertheless, it will rapidly change depending on the gas mixture and pretreatments, and we do not have an insight in this dynamic evolution. The corresponding Al2p and Fe2p spectra are plotted in **Figure 3** (dotted lines). A 100 nm top layer is etched in order to eliminate the above-mentioned contaminants and oxide layer and to recover a fresh metallic surface. Figure 3 shows the Al 2p XPS and Fe 2p spectra of this surface. The Al:Fe atomic ratio of the film equals 13:4.3; that is slightly Fe-rich as compared to the 13:4 ratio of $Al_{13}Fe_4$ and very close to the upcoming STEM/EDX results (Al(75) Fe(25)) for the top part. The contribution at 72.2 eV in the Al 2p
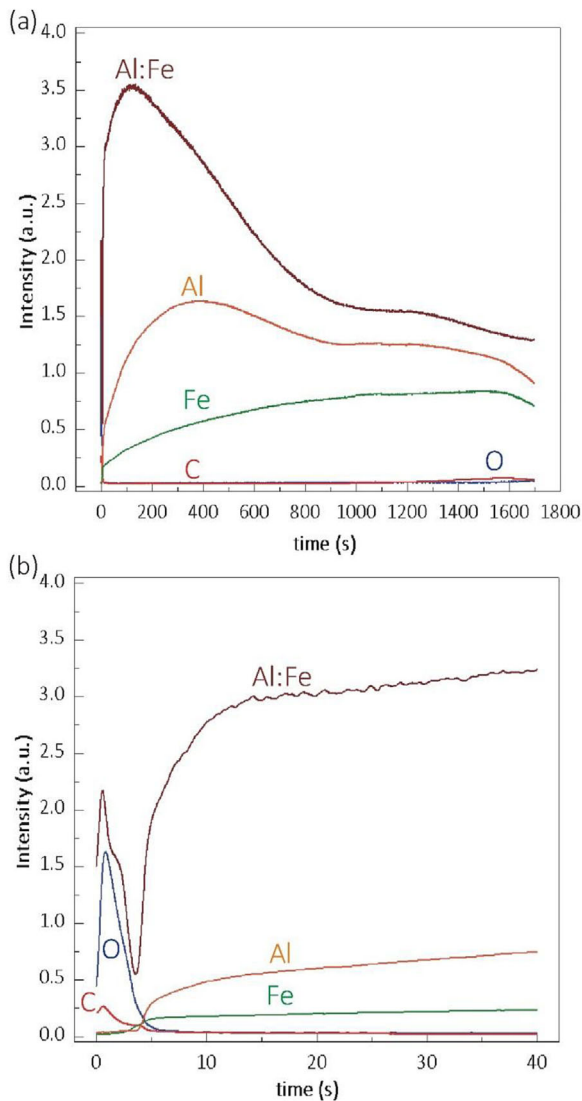
Figure 2. Qualitative depth profiles obtained by GD-OES analysis of an Al-Fe film, (a) through the whole depth of the film and (b) close to the surface.

Figure 3. (a) Al 2p XPS spectrum with Al^0 and Al^{3+} contributions, before (dotted line) and after (full line) ion etching. (b) Fe 2p XPS spectrum compared to a Fe reference, before (dotted line) and after (full line) ion etching.

spectra (Figure 3a) corresponds to metallic Al, while the second signal at ca. 74.6–75.6 eV corresponds to oxidized Al. The oxide contribution decreases with increasing depth before it stabilizes at the level of Figure 3a. This confirms the superficial O contamination observed in GD-OES (Figure 2) and reveals the formation of a surface Al oxide. The oxide cannot be completely avoided due to the exposure of the sample to ambient air, to the relatively high pressure of the XPS chamber (10^{-8} Torr), and to the important open porosity of the films, resulting in superficial Al oxidation through the thickness. The Fe2p peaks ($\Delta BE = 13.1$ eV) are slightly shifted to higher binding energies with regard to the Fe 2p peaks of the reference Fe sheet. This difference is characteristic of the altered electronic structure in intermetallic compounds with transition metals and has also been observed in the Pd-Ga system.[21] Except for the thin contamination layer (O, C species) formed during the exposure of the surface to the
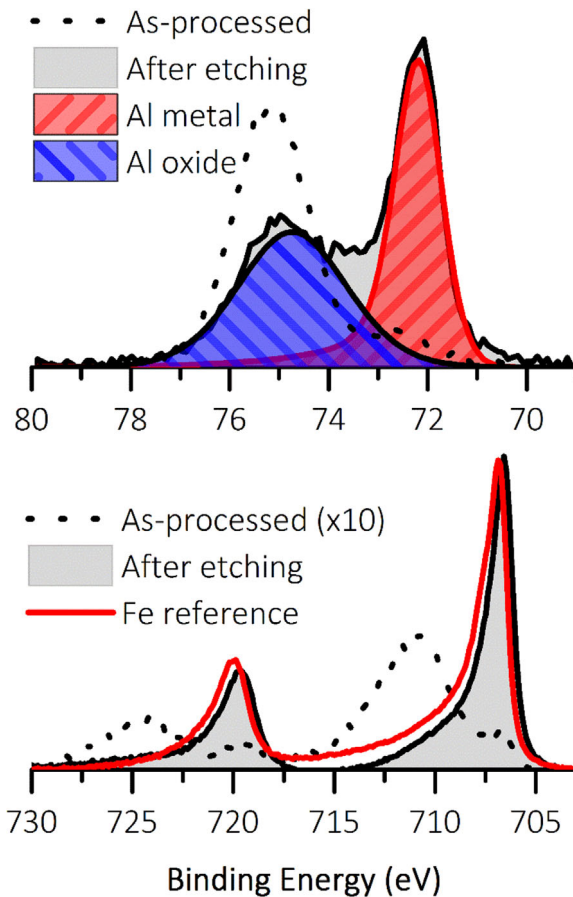
atmosphere, the surface of the coatings is alloyed with the Al:Fe ratio close to that of $Al_{13}Fe_4$.

These results are in good agreement with similar XPS characterizations performed on the surface of a bulk $Al_{13}Fe_4$ sample,[6] where the Fe 2p core-level spectrum presents fine differences such as small shift, decreased half-width and reduced asymmetry from the elemental iron, and the Al 2p spectrum has an Al contribution at 72.5 eV and an Al_2O_3 contribution at 75.5 eV. Overall, it is assumed that the surface is composed of a thin alumina layer formed by the preferential segregation of Al to the surface, but limited enough to prevent the dissolution of the Al-Fe alloy underneath.

Figure 4 corresponds to a film deposited on a glass substrate and subsequently annealed at 575 °C. It shows a SEM image of the lamella prepared by FIB (Figure 4a) and corresponding STEM-EDX elemental maps of the inner (Figure 4b) and the outer (Figure 4c) parts of the film. The film thickness exceeds 15 μm. An important open porosity is observed, further illustrated by SEM cross sectional micrographs shown in Supporting Information. The image has been analyzed using the software nanoTOPO_SEM^{TM} provided by Nanometrisis P.C. The procedure is detailed in Supporting Information.
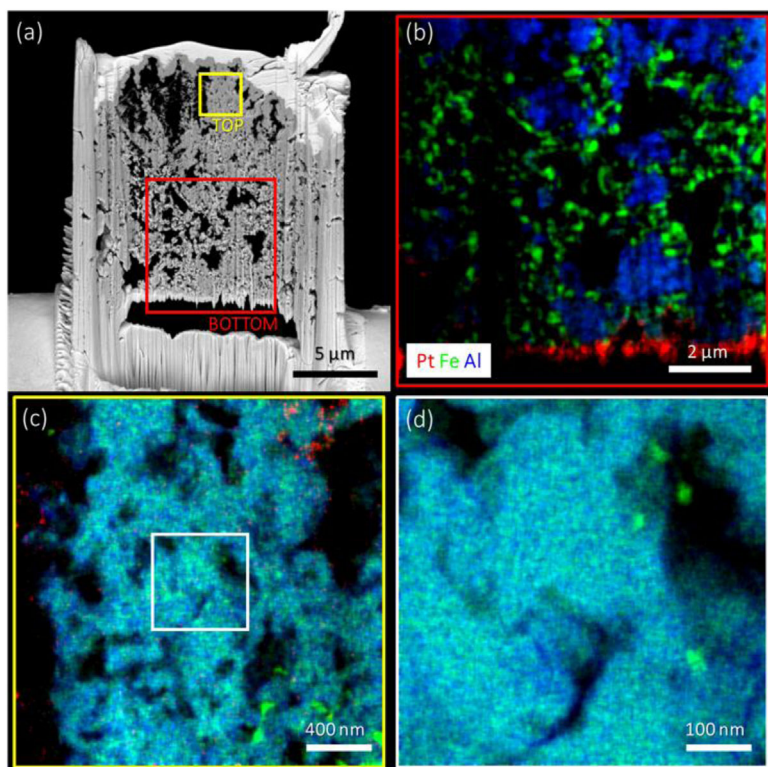
Figure 4. Lamella prepared by FIB (a). STEM-EDX mapping of the bottom (red) square (b) and of the top (yellow) square(c). A higher resolution STEM-EDX is shown within the white square in c (d). Pt is used for brazing the lamella in situ to the manipulator and to protect the interface from curtain effects due to FIB cutting.

Considering a 0.15 threshold of the pixel intensity distribution function, the porosity has been evaluated to be 16–17%. It is attributed to the rough microstructures of the two initial layers, reported in Refs. [18,19] for Al and Fe films, respectively, further perturbed by the extended interdiffusion during annealing. In that lamella, no pure Al regions are observed, confirming that diffusion is effective across the whole stack. The Fe concentration is higher at the interface and decreases up to the surface in agreement with the GD-OES results. For instance, we observe in Figure 4b (red square in Figure 4a) that more than 50 vol.% of the bottom part of the lamella is composed of Fe-rich grains (in green). Local quantitative EDX analysis shows regions with elemental compositions of for example Al(25)Fe(75) or Al(15)Fe(85). Toward the free surface, the fraction of Fe-rich grains decreases until the top 2–3 μm-thick layer where the composition is homogeneous. Figure 4c shows the mapping of the chemical composition in the top region (yellow square of Figure 4a). Except for some Fe-rich inclusions at the bottom, we measure a homogeneous Al(75)Fe(25) matrix composition by quantitative EDX, corresponding to the m-$Al_{13}Fe_4$ composition. A higher resolution map corresponding to the white square of Figure 4c is shown in Figure 4d. A few 20–40 nm wide Al(53)Fe(47) inclusions (bright green contrast) are found. At the edges of the matrix, and surrounding pores, we find an Al content slightly higher than in the matrix (Al(79)Fe(21)). This Al enrichment is correlated with the presence of O. Al preferential oxidation is common in Al-transition metal alloys, and this is in

agreement with the formation of Al oxide at free surfaces as confirmed by XPS measurements (Figure 3 and description thereof). We cannot assess, though, if this oxidation occurs during film formation or ex situ during the lamella preparation/transfer.

A single-grain is characterized by TEM, in **Figure 5**, to further confirm the formation of the $Al_{13}Fe_4$ phase in its monoclinic form. Figure 5a shows an Al-Fe grain (dark grey) that grew laterally from an Al-Fe to an Al region, in the form of a 180 nm-thick rectangle. A high-resolution TEM image of this crystal is shown in Figure 5b. The lattice parameters of 8.0 Å (010) and 7.5 Å (200) measured in this HRTEM image, match the $Al_{13}Fe_4$ lattice parameters. Furthermore, we perform a Fast Fourier Transform (FFT – Figure 5c) of the atomically resolved image in order to identify crystallographic orientations. The indexation of the spots and the zone axis confirms the formation of the m-$Al_{13}Fe_4$ phase (we use the analogous m-$Al_{13}Fe_4$ phase reported in Villars et al.[22]) with the following parameters $a = 15.49$ Å, $b = 8.08$ Å, $c = 12.48$ Å, $\beta = 107.75°$, which are in good agreement with the corresponding parameters reported in previous works.[5]

TEM and STEM investigation of the films deposited sequentially in the conditions of **Table 1** reveals that Fe diffuses toward the interface with silicon oxide or glass, readily at its CVD deposition temperature (not shown). When temperature is increased from the Fe deposition (140 °C) to 575 °C for in situ annealing, a complete transformation to Al-Fe phases occurs in the vicinity of the interface, where Fe rich grains are observed (Figure 4). Such strong diffusion of Fe through the Al sublayer toward the interface may be facilitated by the high concentration of defects, in the form of grain boundaries and porosity. These results as well as XRD observations imply that annealing at 575 °C for 60 min is enough for the formation of the m-$Al_{13}Fe_4$ but not long enough to allow complete homogenization of the composition of the films.

2.2. Semi-Hydrogenation of Acetylene

Figure 6 shows the temperature and the specific activity in the semi-hydrogenation of acetylene (C_2H_2:H_2:He = 2:10:88) of the $Al_{13}Fe_4$–containing catalyst as a function of the time on stream. A catalytic activity is measured from 100 °C and the maximum (about 84% of conversion) is reached around 180 °C. However, the catalyst is rapidly deactivated and its activity is divided by 5 in 15 h. A few traces of C4 products from the acetylene polymerization are measured during the first 100 min of the experiment.

Reductive and oxidative treatments were carried out with the aim to evaluate the possibility to regenerate the catalyst activity by purifying the surface of the $Al_{13}Fe_4$ grains and suppressing the carbon containing by-products formed during the previous catalytic test (cf. below). The reductive treatment consists in a
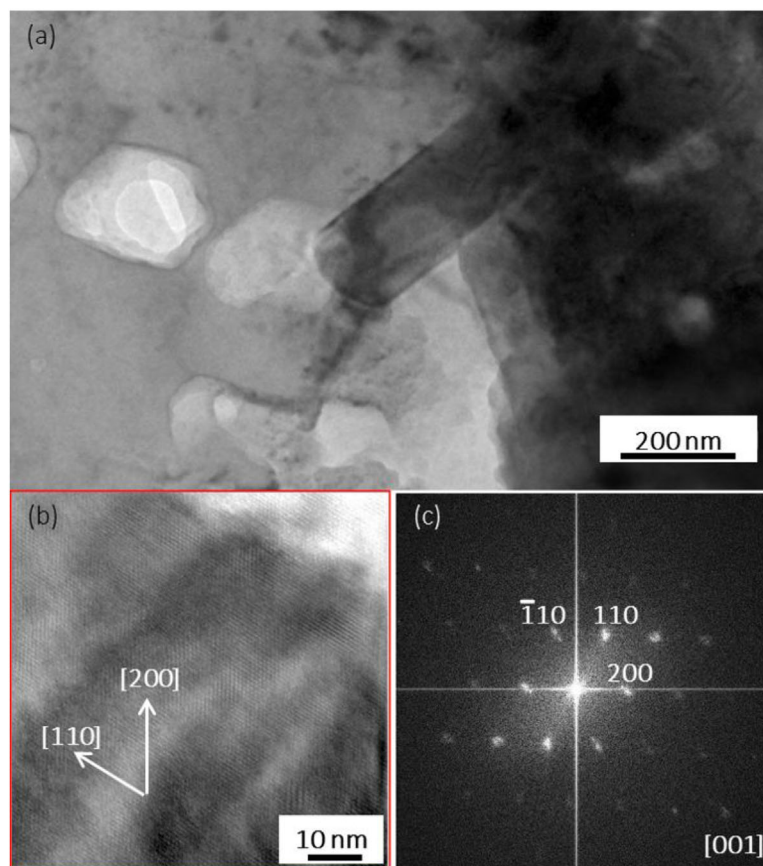
Figure 5. (a) TEM zoom in a $Al_{13}Fe_4$ crystallite. (b) High-resolution TEM image showing the atomic plane arrangement in Al-Fe nanocrystal of b. (c) Indexed fast Fourier transform of image c confirming the formation of m-$Al_{13}Fe_4$ along [001] zone axis.

plateau at 200 °C for 4 h followed by 30 min at 350 °C under H_2 flow while the oxidative treatment is a plateau under O_2 flow at 200 °C for 30 min. Moreover to favor the activity and to counteract the catalyst deactivation the C_2H_2/H_2 ratio was decreased in the feed stream after pre-treatments (i.e., (C_2H_2:H_2: He = 0.5:5:94.5). The activity slightly increases; that is it doubles, especially after the oxidizing treatment which must make it possible to clean the surface more efficiently. However in both cases the catalyst continues to deactivate in spite of a smaller C_2H_2/H_2 ratio.

The initial conversion is 84% but it rapidly drops to 2%. It drops to a slightly higher value of 11% when the catalytic test is performed at 450 °C. The strong deactivation is assumed to originate from the formation of carbonaceous species, revealed by visual observations and XPS. Actually, soot is observed as a black/brown precipitate in the reactor after the catalytic

experiments. Fe is a well-known catalyst for the formation of various carbon based materials, such as soot[23] or carbon nanostructures.[24] It is worth noting that a threefold increase of soot has also been reported in ethylene/oxygen flames after addition of Fe.[25] These carbon residues are not bonded to the surface and are easily removed. On the other hand, XPS spectra (not shown) show a 3 to 6-fold increase of the carbides component of the C1s peak within the film after catalysis. Therefore, we state that the sharp decrease of the conversion is not related to the $Al_{13}Fe_4$ phase where isolated Fe atoms are protected by Al shells; but to other Fe containing phases (Fe, Al_5Fe_2) which catalyze the formation of soot and are deactivated by subsequent carbidization.

Figure 7 shows the selectivity of the $Al_{13}Fe_4$–containing catalyst as a function of the time on stream for the three

Table 1. Operating conditions of the sequential deposition process and obtained dominant phases.

	Deposition time (min)	T_s (°C)	P_d (Torr)	Q_{DMEAA} (sccm)	$Q_{Fe(CO)5}$ (mL min^{-1})	Thermal annealing (min)	Thermal annealing (°C)	Dominant phase
(Al/Fe)	90/5	180/140	5/40	4	0.02	60	500	*fcc* Al/*bcc* Fe
(Al/Fe)	90/5	180/140	5/40	4	0.02	60	550	AlFe/Al_5Fe_2
(Al/Fe)	90/5	180/140	5/40	4	0.02	60	575	$Al_{13}Fe_4$

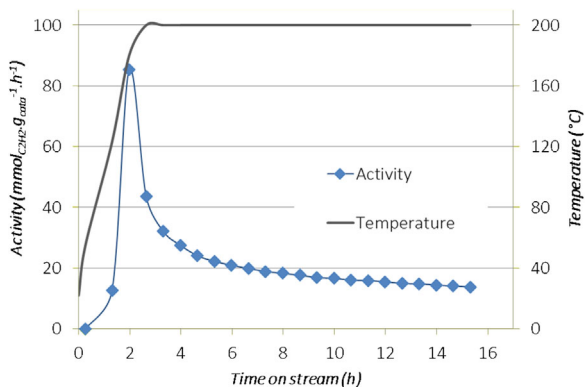**Figure 6.** Reactor temperature and specific activity of a m-$Al_{13}Fe_4$ containing film as a function of time on stream up to 15 h for the ethylene production. C_2H_2:H_2:He = 2:10:88, the total flow rate is 50 mL s^{-1} and the weighted-hourly space velocity (WHSV) equals 3.9 h^{-1}.

sequential experiments. The beginning of the recording for each curve corresponds to the time when the temperature of the bench attains 200 °C. For the as-processed sample, the selectivity in ethylene starts at 81–82%; it continuously decreases and is stabilized at ca. 74% after 2 h at 200 °C, until the end of the test corresponding to 15 h of operation. As expected, the selectivity slightly decreases for the two experiments carried out with a smaller C_2H_2/H_2 ratio; more precisely it decreases to constant value of ca. 71% for the reductive treatment. In contrast, it suffers significantly on treating the catalytic film in O_2 at 200 °C where it caps at 61%. The present selectivity measurements are comparable with the values (81–84%), reported by Armbruster et al. on pure, unsupported $Al_{13}Fe_4$ powders.[6] Similar to our results, the authors also observed that the H_2 and especially the oxidizing treatments result in decreased selectivity.
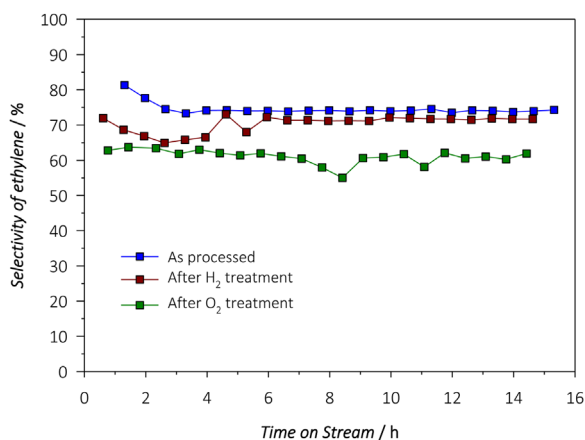

Figure 7. Selectivity of the ethylene production on a m-$Al_{13}Fe_4$ containing film as a function of time on stream up to 15 h. Blue data correspond to a first experiment on as processed film. Brown data to a subsequent experiment performed after regeneration of the catalyst under H_2 flow. Green data correspond to a final experiment after oxidative treatment in O_2 flow.

3. Conclusions

The sequential chemical vapor deposition of Al/Fe bilayers from DMEAA and Fe(CO)$_5$, respectively, followed by in situ post deposition annealing resulted, for the first time of films containing the approximant m-$Al_{13}Fe_4$ phase as demonstrated by XRD, and zone axis indexation and determination of interatomic parameters in HRTEM micrographs. GD-OES and STEM/EDX reveal that the 15 µm thick films present a composition gradient from the Al-rich surface to the Fe-rich interface with the silicon oxide substrate and are globally slightly over stoichiometric in Fe with regard to the targeted Al:Fe = 13:4 ratio. They contain a significant open porosity which has been developed during the reactive interdiffusion of the two metals. XPS measurements indicate the peculiar position of the Fe 2p peak corresponding to that in the $Al_{13}Fe_4$ phase and confirm that the formation of a thin passivating layer of Al oxide does not impact the $Al_{13}Fe_4$ phase underneath.

Catalytic tests with these materials for the semi-hydrogenation of acetylene show selectivity to ethylene as high as 74% over 15 h time on stream, close to the reported values for pure, unsupported $Al_{13}Fe_4$. The initial conversion of 84% rapidly drops due to soot production by catalytic reaction of Fe atoms on acetylene, and to carbidation. The high selectivity and especially the poor conversion are expected to be improved by engineering the CVD process and the annealing conditions so as to obtain $Al_{13}Fe_4$ films with still high specific surface but exempted from Fe-rich phases.

4. Experimental Section

Depositions are performed in a vertical, cylindrical, stagnant flow, cold wall, stainless steel CVD reactor as described in detail[26] and modeled[17,27] in previous works. Substrates are 20 × 12 × 2 mm^3 glass and 10 × 10 × 1 mm^3 thermally oxidized Si coupons in order to avoid the formation of silicides (if Si substrates are used). The substrates are sonicated in acetone and ethanol for 5 min, dried under pure Ar stream and baked at 60 °C for 30 min. They are weighted using a microbalance (Sartorius) before and after deposition for the determination of the mass gain (±1 µg) over the experiment duration, thus providing a mean value of the deposition rate for every set of process conditions. In each experiment five substrates are placed horizontally at different radial positions, on a 58 mm diameter susceptor (substrate holder) heated by a resistance coil gyred just below the surface. A homogeneous gas distribution is ensured by a perforated shower plate facing the substrates.[28] Gases flow rates are controlled by mass flow controllers (MKS).

Al films are formed by the decomposition of the liquid precursor dimethylethylamine alane (DMEAA), provided by NanoMePS (www.nanomeps.fr, last accessed November 28, 2017). For all deposition experiments the DMEAA containing bubbler is thermally regulated at 7 °C, where its saturated vapor pressure is 0.7 Torr.[29] During the deposition of the Al film, N_2 (99.9992% Air Products) flows through DMEAA ($Q_{N2,DMEAA}$ = 25 standard cubic centimeters, sccm) and as dilution gas (Q_{N2} = 325 sccm). The maximum flow rate of DMEAA in these conditions equals 2 sccm.[30] Films processed at low deposition temperature, T_d ca. 140 °C show scattered grains on the surface and form rough morphologies with poor uniformity and no continuity. By increasing T_d grains coalesce and the density of the film increases. Details of the microstructure and the growth rate of the Al films have been reported in Ref. [17].

Fe films are processed from iron pentacarbonyl (Fe(CO)$_5$), a high saturated vapor pressure liquid precursor which yields pure Fe films with

C and O contaminants at the level of a few at%.[31] Fe(CO)$_5$ (>99.99%, Sigma–Aldrich) is transported to the deposition area by direct liquid injection (DLI − Vapbox^{TM}, Kemstream). Small batches of 4 mL of pure Fe(CO)$_5$ are used thus limiting storage degradation. DLI conditions result in a controlled flow rate of 0.02 mL min^{-1} of Fe(CO)$_5$ in the reactor chamber. As for the Al films, low T$_d$ ca. 130 °C results in Fe deposition in the form of scattered grains on the surface and in films with poor uniformity and no continuity. With increasing T$_d$ faceted Fe larger grains start to form and the density of the film increases because of grains coalescence. At T$_d$ higher than 170 °C angular and sharply-faceted grains are first formed followed by films with an acicular morphology above 200 °C. Details on the microstructure and the growth rate of the Fe films can be found in Ref. [19].

Based on these results on the growth rate and on the microstructure of the two elements, bi-layers were processed by first depositing Al at T$_d$ and P$_d$ 180 °C and 5 Torr followed by deposition of Fe at 140 °C and 40 Torr.

Post-deposition annealing is applied to the Al/Fe bilayers immediately after deposition to stimulate reactive diffusion. It is performed in situ for 60 min, at different temperatures, under primary vacuum of 1×10^{-1} Torr, thus limiting the contamination of the films. The choice of the range of the annealing temperature is based on the Al–Fe phase diagram[33] and on the results reported on the formation of Al–Fe intermetallic phases determined by high-temperature XRD.[11] However, results are shown only for 575 °C, since the intermetallic Al$_{13}$Fe$_4$ phase is only formed at this temperature. The conditions of sequential depositions and the dominant phases obtained by annealing at 3 different temperatures are summarized in Table 1.

Elemental depth profiles are determined by radio frequency GD-OES with a Horiba Scientific GD-Profiler2. Due to the absence of calibration curves, only qualitative trends are obtained. X-ray photoelectron spectroscopy (XPS) measurements are performed on a Thermo Scientific K-Alpha instrument using monochromatic Al Kα (1486.6 eV) radiation. The ion etching rate (Ar$^+$, 2 kV) is ca. 0.08 nm s^{-1}. High resolution scans are obtained at constant pass energy of 30 eV with energy steps of 0.1 eV. Atomic concentrations are determined from photoelectron peak areas using the atomic sensitivity factors reported by Scofield, taking into account the transmission function of the analyzer. Compositional maps at the nm scale are obtained with scanning transmission electron microscopy (STEM) coupled with Energy Dispersive X-Ray measurements (EDX). STEM is performed using a FEI Titan 80–200 (ChemiSTEM) electron microscope[32] operating at 200 kV, equipped with a spherical-aberration (Cs) probe corrector (CEOS GmbH), and a high-angle annular dark field (HAADF) detector. A probe semi-angle of 25 mrad and an inner collection semi-angle of the detector of 88 mrad are used. Elemental analysis is performed using four large-solid-angle symmetrical Si drift detectors. For EDX analysis, Fe K and Al K peaks are used. Crystallographic structures are determined by X-ray diffraction (XRD) on a SEIFERT-3000TT instrument using a Cu K$_\alpha$ (1.5418 Å) X-ray tube operated at 40 kV and 40 mA, a Ni filter and solid-state Lynxeye detector. Diffraction patterns were acquired with a 2θ step size of 0.25° over a 2θ range of 0–120°. Surface morphology is observed using scanning electron microscopy (SEM) on a LEO 435VP instrument. Cross section micrographs of selected samples are prepared and observed with a FEI Helios 600i station composed of a focused ion beam (FIB) and a field emission gun (FEG) SEM, operating at 5 kV. Transmission eletron microscopy (TEM) coupled with EDX measurements is performed with a JEOL JEM 2100F high resolution microscope operating at 200 kV and equipped with a BRUKER EDX spectrometer for chemical analysis. High resolution TEM (HR-TEM) analysis is also performed in the same instrument for crystallographic characterizations of the Al$_{13}$Fe$_4$ crystal. TEM lamellas are prepared by FIB.

Catalytic tests for the semi-hydrogenation of acetylene are carried out at 200 °C under atmospheric pressure in a continuous flow fixed-bed reactor which consists of a cylindrical glass tube of 16 mm diameter equipped with a sintered glass filter to support the catalyst. The reactor is placed in a ceramic furnace and the temperature is controlled via a thermocouple. The reactive gases (C$_2$H$_2$:H$_2$:He) are mixed using mass flow controllers (Brooks and Vögtlin) with a ratio 2:10:88, respectively and

flowing through the reactor with a total rate of 50 sccm. The effluent gases are analyzed online using Shimadzu GC-2014 gas chromatograph equipped with a Supelco alumina sulfate plot coupled with a silica capillary column and a FID detector. Large samples were synthesized in the same conditions on thermally grown silica on Si substrates, in order to provide 25 mg equivalent of Al$_{13}$Fe$_4$ containing film. Samples are crushed with the aim to mimic the deposition of a supported catalyst on a powder substrate. The powder is then introduced in the catalytic reactor. The set-up is placed on the test bench under N$_2$ atmosphere while avoiding contact of the catalyst with O$_2$ and moisture.

[1] W. R. True, *Oil Gas J.* Vol. *111*, PennWell Petroleum Group, Huston, TX **2013**, p. 90.

[2] F. Studt, F. Abild-Pedersen, T. Bligaard, R. Z. Sorensen, C. H. Christensen, J. K. Norskov, *Science* **2008**, *320*, 1320.

[3] G. Kyriakou, M. B. Boucher, A. D. Jewell, E. A. Lewis, T. J. Lawton, A. E. Baber, H. L. Tierney, M. Flytzani-Stephanopoulos, E. C. H. Sykes, *Science* **2012**, *335*, 1209.

[4] P. J. Black, *Acta Crystallogr.* **1955**, *8*, 43.

[5] M. Ellner, *Acta Crystallogr. B* **1995**, *51*, 31; J. Grin, U. Burkhardt, M. Ellner, K. Peters, *Z. Kristallogr.* **1994**, *209*, 479.

[6] M. Armbruster, K. Kovnir, M. Friedrich, D. Teschner, G. Wowsnick, M. Hahne, P. Gille, L. Szentmiklosi, M. Feuerbacher, M. Heggen, F. Girgsdies, D. Rosenthal, R. Schlogl, Y. Grin, *Nat. Mater.* **2012**, *11*, 690.

[7] M. Armbruster, G. Wowsnick, M. Friedrich, M. Heggen, R. Cardoso-Gil, *J. Am. Chem. Soc.* **2011**, *133*, 9112; H. R. Zhou, X. F. Yang, L. Li,

X. Y. Liu, Y. Q. Huang, X. L. Pan, A. Q. Wang, J. Li, T. Zhang, *ACS Catal.* **2016**, *6*, 1054; T. Ghosh, B. M. Leonard, Q. Zhou, F. J. DiSalvo, *Chem. Mater.* **2010**, *22*, 2190.

[8] J. Ledieu, E. Gaudry, L. N. S. Loli, S. A. Villaseca, M. C. de Weerd, M. Hahne, P. Gille, Y. Grin, J. M. Dubois, V. Fournee, *Phys. Rev. Lett.* **2013**, 110.

[9] Q. C. Feng, S. Zhao, Y. Wang, J. C. Dong, W. X. Chen, D. S. He, D. S. Wang, J. Yang, Y. M. Zhu, H. L. Zhu, L. Gu, Z. Li, Y. X. Liu, R. Yu, J. Li, Y. D. Li, *J. Am. Chem. Soc.* **2017**, *139*, 7294.

[10] A. Csanady, J. R. Gunter, P. B. Barna, J. Mayer, *Thin Solid Films* **1988**, *167*, 203; S. R. Teixeira, C. A. Dossantos, P. H. Dionisio, W. H. Schreiner, I. J. R. Baumvol, *Mat. Sci. Eng.* **1987**, *96*, 285; S. R. Teixeira, F. L. Freire, I. J. R. Baumvol, *Appl. Phys. A: Mater. Sci. Process.* **1989**, *48*, 481.

[11] F. Haidara, M. C. Record, B. Duployer, D. Mangelinck, *Intermetallics* **2012**, *23*, 143.

[12] S. Kumar, V. Selvarajan, P. V. A. Padmanabhan, K. P. Sreekumar, *Surf. Coat. Technol.* **2006**, *201*, 1267; G. J. Yang, H. T. Wang, C. J. Li, C. X. Li, *Surf. Coat. Technol.* **2011**, *205*, 5502.

[13] A. Canakci, F. Erdemir, T. Varol, S. Ozkaya, *Powder Techn.* **2013**, *247*, 24.

[14] C. Vahlas, *Complex Metallic Alloys: Surfaces and Coatings*, E. Belin-Ferré (Ed.), World Scientific, Singapore **2010**, p. 49.

[15] N. Prud'homme, T. Duguet, D. Samélor, F. Senocq, C. Vahlas, *Appl. Surf. Sci.* **2013**, *283*, 788.

[16] Y. Zhang, B. A. Pint, K. M. Cooley, J. A. Haynes, *Surf. Coat. Technol.* **2008**, *202*, 3839; J. T. John, R. S. Srinivasa, P. K. De, *Thin Solid Films* **2004**, *466*, 339; Z. D. Xiang, P. K. Datta, *Surf. Coat. Technol.* **2004**, *184*, 108.

[17] I. G. Aviziotis, T. Duguet, K. Soussi, G. Kokkoris, N. Cheimarios, C. Vahlas, A. G. Boudouvis, *Phys. Status Solidi C* **2015**, *12*, 923.

[18] I. G. Aviziotis, N. Cheimarios, T. Duguet, C. Vahlas, A. G. Boudouvis, *Chem. Eng. Sci.* **2016**, *155*, 449.

[19] I. G. Aviziotis, T. Duguet, C. Vahlas, A. G. Boudouvis, *Adv. Mater. Interfaces* **2017**, 1601185.

[20] D. Naoi, M. Kajihara, *Mat. Sci. Eng. A* **2007**, *459*, 375.

[21] K. Kovnir, M. Armbruster, D. Teschner, T. V. Venkov, L. Szentmiklosi, F. C. Jentoft, A. Knop-Gericke, Y. Grin, R. Schlogl, *Surf. Sci.* **2009**, *603*, 1784.

[22] P. Villars, *Handbook of Ternary Alloy Phase Diagrams*, ASM International, Materials Park, OH **1995**.

[23] J. H. Hahn, N. M. Hwang, D. Y. Yoon, *J. Mat. Sci. Lett.* **1996**, *15*, 1240.

[24] R. Marangoni, P. Serp, R. Feurer, Y. Kihn, P. Kalck, C. Vahlas, *Carbon* **2001**, *39*, 443.

[25] A. S. Feitelberg, J. P. Longwell, A. F. Sarofim, *Combust. Flame* **1993**, *92*, 241.

[26] T. C. Xenidou, A. G. Boudouvis, N. C. Markatos, D. Samélor, F. Senocq, A. N. Gleizes, N. Prud'homme, C. Vahlas, *Surf. Coat. Technol.* **2007**, *201*, 8868.

[27] I. G. Aviziotis, N. Cheimarios, C. Vahlas, A. G. Boudouvis, *Surf. Coat. Technol.* **2013**, *230*, 273.

[28] T. C. Xenidou, N. Prud'homme, C. Vahlas, N. C. Markatos, A. G. Boudouvis, *J. Electrochem. Soc.* **2010**, *157*, D633.

[29] D. M. Frigo, G. J. M. Vaneijden, P. J. Reuvers, C. J. Smit, *Chem. Mater.* **1994**, *6*, 190.

[30] S. D. Hersee, J. M. Ballingall, *J. Vac. Sci. Technol.* **1990**, *A8*, 800.

[31] R. B. Jackman, J. S. Foord, *Surf. Sci.* **1989**, *209*, 151.

[32] A. Kovács, R. Schierholz, K. Tillmann, *JLSRF* **2016**, *2*, 1